

# Atomic Mass Dependence of Hadron Production in Deep Inelastic Scattering on Nuclei

A. Accardi<sup>a,b</sup>, D. Grünewald<sup>c,1</sup>, V. Muccifora<sup>d</sup> and  
H.J. Pirner<sup>c</sup>

<sup>a</sup>*Columbia Physics Department, 538 West 120th Street, New York, NY 10027, U.S.A.*

<sup>b</sup>*Iowa State University, Dept. of Physics and Astrophysics, Ames, IA 50011, U.S.A.*

<sup>c</sup>*Institut für Theoretische Physik der Universität Heidelberg Philosophenweg 19, D-69120 Heidelberg, Germany*

<sup>d</sup>*INFN, Laboratori Nazionali di Frascati, I-00044 Frascati, Italy*

---

## Abstract

Hadron production in lepton-nucleus deep inelastic scattering is studied in an absorption model. In the proposed model, the early stage of hadronization in the nuclear medium is dominated by prehadron formation and absorption, controlled by flavor-dependent formation lengths and absorption cross sections. Computations for hadron multiplicity ratios are presented and compared with the HERMES experimental data for pions, kaons, protons and antiprotons. The mass-number dependence of hadron attenuation is shown to be sensitive to the underlying hadronization dynamics. Contrary to common expectations for absorption models, a leading term proportional to  $A^{2/3}$  is found. Deviations from the leading behavior arise at large mass-numbers and large hadron fractional momenta.

*Key words:*

*PACS:* 12.38.-t, 13.60.Hb, 13.60 Le

---

<sup>1</sup> Corresponding author. E-mail address: daniel@tphys.uni-heidelberg.de

## 1 Introduction

Recent HERMES results give precise data on hadron production in deep inelastic scattering (DIS) of 27.6 GeV positrons on D, He, N, Ne, and Kr nuclei [1–3]. The main observable is the multiplicity ratio,  $R_M$ , defined as the ratio between the hadron multiplicity on nucleus and on deuterium.  $R_M$  has been studied as a function of the hadron fractional momentum  $z$ , of the virtual photon energy  $\nu$ , of its virtuality  $Q^2$ , for different hadrons and for different nuclei. The use of nuclear targets allows to study the hadronization process near the interaction point of the photon and probe hadron formation only some fermi away.

There are many proposed models to describe how hadronization in presence of a nucleus evolves in space and time. The model computations range from a color string breaking mechanism [4–6,9,7,8] with final state interaction [10,11], to gluon bremsstrahlung for leading hadrons [12,13] and pure energy loss models [14–16]. Two classes of models of hadron formation compete with each other. The first one is based on nuclear absorption, where the color of the struck quark is neutralized after a short time by the formation of a prehadron, the predecessor of the final hadron, which interacts with surrounding nucleons and is absorbed on its way out of the nucleus. The second model assumes energy loss from medium-induced radiation of the struck quark as dominant process. The first interpretation emphasizes the hadronic aspects of particle production, the second one focuses on partonic degrees of freedom and postpones hadronization outside the nucleus. Both mechanisms reduce the number of hadrons emerging from the nucleus. The current belief is that the dependence of hadron attenuation from the mass-number  $A$  of the target nucleus can differentiate the two processes: in the absorption model, hadron attenuation is commonly believed to be proportional to the path length of the (pre)hadron in the nucleus ( $\propto A^{1/3}$ ), whereas in the energy loss model the attenuation is supposed to depend on the square of the distance the quark traverses in the nucleus ( $\propto A^{2/3}$ ). A careful measurement of the  $A$ -dependence of the nuclear attenuation would therefore allow to discriminate between the two different processes.

In a previous paper [17], we have calculated the nuclear modifications of hadron production in DIS in an absorption model. The hadron formation length has been computed analytically in the framework of the Lund string model [5,18] as a two-step process. In the first step a quark-antiquark pair from the break-up of the color string forms a prehadron. In the second step the final state hadron is created. Both the prehadron and the hadron, if they form inside the nucleus, interact with target nucleons and may be absorbed. Setting the prehadron nucleon cross section equal to the hadron nucleon cross section in Ref. [17] we had to increase the formation length by using an ef-

fective string tension  $\kappa=0.4$  GeV/fm, much smaller than the expected  $\kappa \approx 1$  GeV/fm (see Ref. [19] for example).

In this paper we correct the model by combining a realistic formation length based on the expected string constant with smaller prehadronic cross sections. We pay special attention to the flavor dependence of the formation length, which is naturally induced by the Lund model, and calculate the multiplicity ratio  $R_M^h$  for different hadron species  $h$  as functions of kinematic variables  $z$  and  $\nu$ . Finally, we study the  $A$ -dependence of the nuclear attenuation  $1 - R_M^h$ , and challenge common expectations by showing, analytically and numerically, a  $A^{2/3}$  dependence for the absorption model.

The paper is organized as follows. In section 2, the new developments of the model are described. Section 3 is devoted to the analytic calculation of the  $A$ -dependence of hadron attenuation. In Section 4, numerical computations of  $R_M^h$  and of the  $A$ -dependence of  $1 - R_M$  are presented and compared with experimental data. Section 5 presents a summary and our conclusions.

## 2 Development of the model

In this section we report the main developments of the model, which has been extensively described in Ref. [17]. The experimental multiplicity ratio  $R_M^h$  between nucleus and deuterium is a double ratio and can be measured as a function of  $z$ ,  $\nu$  or  $Q^2$ . As a function of  $z$  it is given by:

$$R_M^h(z) = \frac{1}{N_A^{DIS}} \frac{dN_A^h(z)}{dz} \Big/ \frac{1}{N_D^{DIS}} \frac{dN_D^h(z)}{dz}. \quad (1)$$

The upper ratio is the number of produced hadrons of species  $h$  with energy fraction  $z$ , normalized to the total number of deep inelastic scattering events on a nuclear target with mass number  $A$ . The lower ratio is the corresponding expression for a deuterium target. The theoretical calculation of the hadron multiplicity on a nucleus  $A$  is based on the computation of the hadron survival probability  $S_{f,h}^A$  and the fragmentation function  $D_f^h$  in the nucleus:

$$\begin{aligned} \frac{1}{N_A^{DIS}} \frac{dN_A^h(z)}{dz} &= \frac{1}{\sigma^{lA}} \int_{\text{exp. cuts}} dx d\nu \\ &\times \sum_f e_f^2 q_f^A(x, \xi_A Q^2) \frac{d\sigma^{lq}}{dxd\nu} S_{f,h}^A(z, \nu) D_f^h(z, \xi_A Q^2). \end{aligned} \quad (2)$$

The total lepton-nucleus DIS cross section  $\sigma^{lA}$  is calculated in leading order by an integration over the parton distribution functions  $q_f$  and the lepton-quark

cross section  $d\sigma^{lq}/dxd\nu$ , including the experimental cuts:

$$\sigma^{lA} = \int_{\text{exp. cuts}} dxd\nu \sum_f e_f^2 q_f^A(x, \xi_A Q^2) \frac{d\sigma^{lq}}{dxd\nu}. \quad (3)$$

The theoretical calculation in Eqs. (2-3) takes into account several nuclear effects. The partial deconfinement model [20] is used to express the nuclear parton distribution function and the nuclear fragmentation function: both the free-nucleon parton distribution function  $q_f(x, Q^2)$  and the free-nucleon fragmentation function  $D_f^h(z, Q^2)$  are rescaled with a factor  $\xi_A = \xi_A(Q^2)$  due to the hypothesis that quarks in a bound nucleon have access to a larger region in space than in free nucleons, i.e.

$$\lambda_A > \lambda_0 \quad (4)$$

where  $\lambda_A$  is the confinement scale of a bound nucleon, which is assumed to be proportional to the overlap of nucleons inside the given nucleus, and  $\lambda_0$  is the confinement scale of a free nucleon. Details are presented in [17].

The hadron survival probability  $S_{f,h}^A$  represents the probability that the hadron emerges from the nucleus without having interacted with the nucleus during its evolution from the quark to its final state. The survival probability depends on the struck quark flavor  $f$ , the hadron species  $h$  and the target nucleus  $A$ . For simplicity, any scattering of the prehadron with a target nucleon is assumed to lead to absorption. In principle the observed hadron with energy fraction  $z$  might have undergone several inelastic rescatterings before being absorbed, whereby its  $z$  is degraded. However, these multiple scattering processes are suppressed at large  $z$  since the fragmentation function is rapidly falling at  $z \rightarrow 1$ , and are expected to be negligible at  $z \gtrsim 0.3 - 0.4$ . In order to calculate  $S_{f,h}^A$  we modify the simplistic Bialas-Chmaj [6] absorption formulae used in Ref. [17], which considers the hadronization process to be a decay process, by fully coupling the evolution of the quark into a prehadron and a hadron with the absorption processes. The quark decays into the prehadron with an average formation length  $\langle l^* \rangle$  after the interaction of the virtual photon  $\gamma^*$  with a quark  $q$ . The prehadron itself decays into the hadron with an average formation length  $\langle \Delta l \rangle$  given by the difference of the average hadron and the average prehadron formation lengths:

$$\langle \Delta l \rangle = \langle l^h \rangle - \langle l^* \rangle \quad (5)$$

Here we omit for ease of notation the dependence of the prehadron and hadron formation length on the struck quark flavor  $f$ , the hadron species  $h$ , the energy fraction  $z$  and the virtual photon energy  $\nu$ . We will come back later on this topic. If the initial  $\gamma^*q$  interaction occurs at longitudinal coordinate  $y$ , the probabilities that the intermediate state at time  $y'$  is a quark,  $P_q(y, y')$ , a

prehadron,  $P_*(y, y')$ , or a hadron,  $P_h(y, y')$ , satisfy the following differential equations:

$$\begin{aligned}\frac{\partial P_q(y, y')}{\partial y'} &= -\frac{P_q(y, y')}{\langle l^* \rangle} \\ \frac{\partial P_*(y, y')}{\partial y'} &= \frac{P_q(y, y')}{\langle l^* \rangle} - \frac{P_*(y, y')}{\langle \Delta l \rangle} - \frac{P_*(y, y')}{\lambda_*(y')} \\ \frac{\partial P_h(y, y')}{\partial y'} &= \frac{P_*(y, y')}{\langle \Delta l \rangle} - \frac{P_h(y, y')}{\lambda_h(y')}\end{aligned}\quad (6)$$

with initial conditions

$$\begin{aligned}P_q(y, y' = y) &= 1 \\ P_*(y, y' = y) &= 0 \\ P_h(y, y' = y) &= 0.\end{aligned}$$

The mean free path of the prehadron  $\lambda_*(y')$  and the mean free path of the hadron  $\lambda_h(y')$  are:

$$\lambda_{*,h}(y') = \frac{1}{A\rho_A(y')\sigma_{*,h}} \quad (7)$$

where  $\rho_A$  is the nuclear density normalized to unity and  $\sigma_{*,h}$  are the respective cross sections of a prehadron and of a hadron. The dependence of  $\rho_A$  on the impact parameter  $b$  is suppressed to simplify the notation. The solutions for the probabilities  $P_q, P_*, P_h$  can be obtained analytically:

$$P_q(y, y') = e^{-\frac{y'-y}{\langle l^* \rangle}} \quad (8)$$

$$P_*(y, y') = \int_y^{y'} dx \frac{e^{-\frac{x-y}{\langle l^* \rangle}}}{\langle l^* \rangle} e^{-\frac{y'-x}{\langle \Delta l \rangle}} e^{-\sigma_* \int_x^{y'} ds A \rho_A(s)} \quad (9)$$

$$P_h(y, y') = \int_y^{y'} dx' \int_y^{x'} dx \frac{e^{-\frac{x-y}{\langle l^* \rangle}}}{\langle l^* \rangle} e^{-\sigma_* \int_x^{x'} ds A \rho_A(s)} \frac{e^{-\frac{x'-x}{\langle \Delta l \rangle}}}{\langle \Delta l \rangle} e^{-\sigma_h \int_{x'}^{y'} ds A \rho_A(s)}. \quad (10)$$

We define the survival probability  $S_{f,h}^A$  of the hadron as the probability that the hadron is not absorbed by the nucleus. It is obtained as  $\lim_{y' \rightarrow \infty} P_h(y, y')$  after integration over all  $\gamma^* q$  interaction points and impact parameters:

$$\begin{aligned}S_{f,h}^A &= \int d^2 b \int_{-\infty}^{\infty} dy \rho_A(b, y) \int_y^{\infty} dx' \int_y^{x'} dx \\ &\times \frac{e^{-\frac{x-y}{\langle l^* \rangle}}}{\langle l^* \rangle} e^{-\sigma_* \int_x^{x'} ds A \rho_A(s)} \frac{e^{-\frac{x'-x}{\langle \Delta l \rangle}}}{\langle \Delta l \rangle} e^{-\sigma_h \int_{x'}^{\infty} ds A \rho_A(s)}.\end{aligned}\quad (11)$$

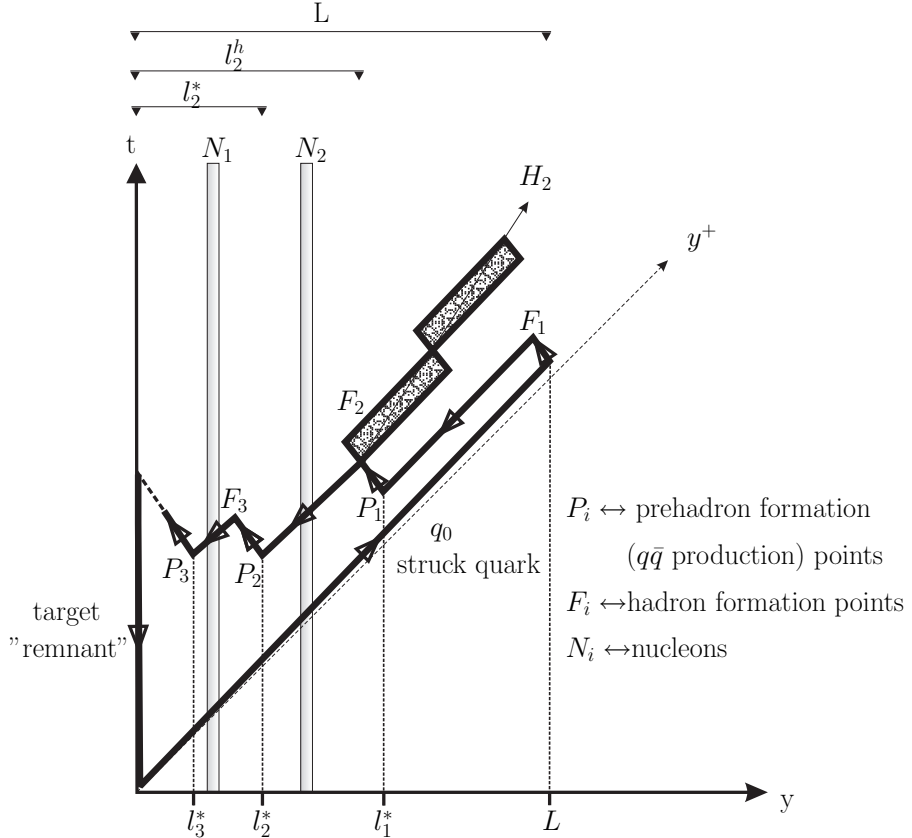


Fig. 1. Schematic space time picture of hadronization in the LUND model.

The formation lengths are computed in the framework of the Lund model [18,5], for which we show a schematic space-time picture in Fig. 1. The target nucleons  $N_1, N_2$  are at rest in the laboratory frame. Since the struck quark and the leading hadrons move close to the light cone, we have enlarged in our illustration the negative light cone momenta and diminished the positive ones for clarity. Furthermore, all masses have been neglected. The hadrons  $H_i$  are formed at the points  $F_i$  and the index  $i$  gives their rank, counted from right to left. The "production" points  $P_i$  are the formation points of the  $i$ -th rank prehadron. The distance  $L$  from the struck quark turning point to the  $\gamma^*q$  interaction point sets the scale of hadronization and is proportional to the energy transferred to the quark:

$$L = \frac{\nu}{\kappa} \quad (12)$$

For the calculation in this paper we use the expected vacuum string constant [4,9,7,19]

$$\kappa = 1 \text{ GeV/fm} . \quad (13)$$

In order to be consistent with the partial deconfinement model, we rescale

the vacuum string constant in the nucleus. Since the string constant is the physical quantity that sets the confinement scale, a larger confinement scale corresponds to a smaller string tension in the nucleus:

$$\kappa_A = \frac{\lambda_0^2}{\lambda_A^2} \kappa . \quad (14)$$

In addition, we explicitly consider the dependence of the formation time on hadron species. The rank 1 hadron has the struck quark as one of its constituents. Therefore, the type of particles which can be produced as a rank 1 depends on the flavor of the struck quark. Negative kaons ( $K^- = s\bar{u}$ ), as well as antiprotons ( $\bar{p} = \bar{u}\bar{u}\bar{d}$ ), cannot be formed by a struck valence quark in the nucleon. They can only be formed from struck sea quarks, which are subdominant at HERMES, or from quarks formed inside the color string. In Fig. 2 we show the different processes which lead to the production of a  $K^+$  and  $K^-$  meson from a struck  $u$  quark. The positive kaon can be directly formed at rank 1, whereas  $K^-$  needs at least a second quark pair produced, i.e. it can only be produced from rank 2 on. Therefore, the LUND string model naturally produces a flavor-dependent formation time. For details about formation times we refer to Ref. [17]. Here we only show how the mean formation time of a hadron which can be produced from all ranks  $n \geq 1$  differs from the formation time of a hadron which can only be produced from rank 2 on, i.e.  $n \geq 2$ . The average prehadron formation length for hadrons which are producible as first rank particle reads:

$$\langle l_{\geq 1}^* \rangle = \frac{1 + D_a}{1 + C + (D_a - C)z} (1 - z) z L \left[ 1 + \frac{1 + C}{2 + D_a} \frac{(1 - z)}{z^{2+D_a}} {}_2F_1 \left( 2 + D_a, 2 + D_a; 3 + D_a; \frac{z - 1}{z} \right) \right] \quad (15)$$

and the average prehadron formation length for particles which are not producible as a first rank particle is given by:

$$\langle l_{\geq 2}^* \rangle = (1 - z) z L \left[ \frac{1 + D_a}{2 + D_a} \frac{1}{z^{2+D_a}} {}_2F_1 \left( 2 + D_a, 2 + D_a; 3 + D_a; \frac{z - 1}{z} \right) \right] \quad (16)$$

Here  ${}_2F_1$  is the Gauss hypergeometric function, the parameters  $C$  and  $D_a$  with  $a = (q, qq)$  arise from the string fragmentation function  $f(u) \propto (1 - u)^{D_a}$ , which is the probability that the string breaks into two pieces under the creation of a quark-anti-quark pair or a diquark-anti-diquark pair respectively. Furthermore, these parameters select whether a meson ( $a = q$ ) or a baryon ( $a = qq$ ) is produced (see Ref. [17]). Their numerical values are given in Ref.

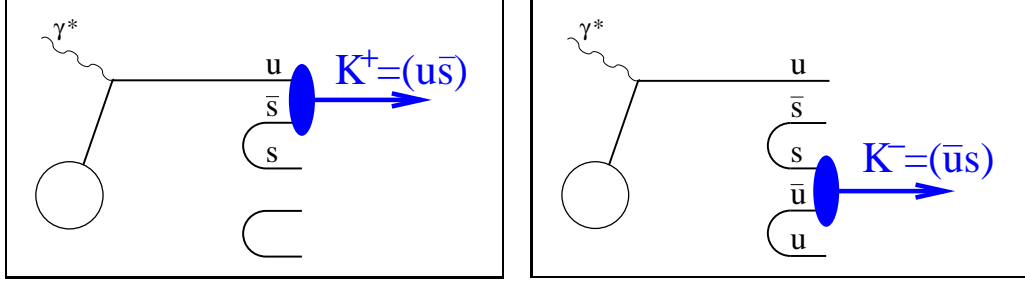


Fig. 2. Schematic picture describing the fragmentation of an up quark into  $K^+$  and  $K^-$ . A similar picture works also for fragmentation into  $p$  and  $\bar{p}$ , respectively.

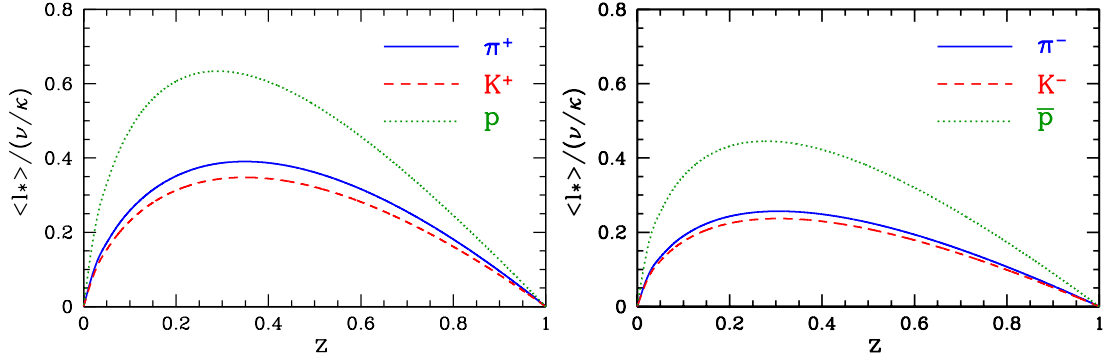


Fig. 3. Computed prehadron formation lengths when an up quark is struck by the virtual photon. *Left:* When a  $\pi^+$ ,  $K^+$  or  $p$  is observed, the corresponding prehadron can be created at rank  $n \geq 1$ . *Right:* When a  $\pi^-$ ,  $K^-$  or  $\bar{p}$  is observed, the corresponding prehadron can be created only at rank  $n \geq 2$ .

[18] by  $C = D_q = 0.3$  and  $D_{qq} = 1.3$ . There is a simple rank-independent connection between the prehadron and the hadron formation length for fixed energy fraction  $z$  carried by the hadron :

$$\langle l_{\geq 1,2}^h \rangle = \langle l_{\geq 1,2}^* \rangle + zL . \quad (17)$$

The present model is based on string fragmentation in (1+1)-dimensions. Realistic hadrons also have a transverse extension. We expect that the prehadron does not yet have the full size of the hadron and therefore interacts with a smaller cross section,  $\sigma_* < \sigma_h$ . We fit the prehadronic cross section to reproduce the pion multiplicity ratio on  $^{84}\text{Kr}$  [2] and we obtain:

$$\sigma_* = \frac{2}{3} \sigma_h . \quad (18)$$

Such a prehadronic cross-section is in agreement with Ref. [11], where the multiplicity ratio of charged hadrons for the HERMES experiment is computed with a prehadronic cross-section increasing quadratically during the hadron formation time  $\tau_f = 0.5 \text{ fm}/c$  from  $0.3\sigma_h$  to the full hadronic cross-section. On the average one obtains a prehadronic cross-section  $\langle \sigma_* \rangle = 0.63\sigma_h$ . We use the proportionality factor 2/3 for all other hadronic species. Empirically

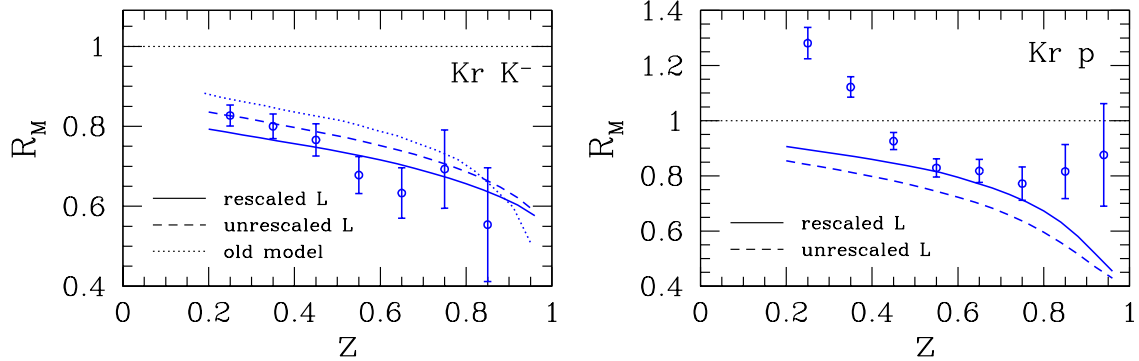


Fig. 4. Multiplicity ratios for  $K^-$  and  $p$  on krypton are shown as function of  $z$  in the left and right panel respectively. Solid (dashed) curves are computed with (without) hadron size rescaling in the formation length. The dotted curve shows the published result [17] for  $K^-$  without the above described model modifications. The data are taken from Ref. [2].

we know that baryons have a larger radius than  $\pi$  mesons, which are larger than  $K$  mesons. Therefore we renormalize the string tension, i.e. the quantity which sets the confinement scale in the Lund model [18,5], to the confinement scales of realistic hadrons, whose values we take from Ref. [21]. Therefore,  $L$  is renormalized to

$$L_h = \frac{\nu}{\kappa} \frac{r_h^2}{r_\pi^2}. \quad (19)$$

for the different hadron species. This produces an increased formation length for baryons due to the larger size of the proton compared with pions. A comparison between the computed formation lengths of pions, kaons, protons and antiprotons is shown in Fig. 3. The flavor dependence decreases the average formation length of the negative mesons by about 30% compared to the positive ones, and by more than 40% for  $\bar{p}$  compared to  $p$ . The effect of the baryon larger size results in a longer baryon formation time compared with the meson ones.

The effect of modified formation length  $L_h$  on the  $K^-$  and  $p$  multiplicity ratios for krypton is shown in the left and right parts of Fig. 4, respectively. The dashed line represents the computation with pion formation length  $L = \nu/\kappa$ , while the solid line shows the effect on the multiplicity ratio of the reduced (increased) formation length for kaons (protons). Thus the modification of the formation length by accounting for hadronic size improves the agreement between the computed and measured multiplicity ratios both for  $K^-$  and  $p$ . In addition, the published results [17] for  $K^-$  without any of the above described model modifications are shown as dotted line. Including in the model a flavor dependent formation length, the realistic string constant and the reduced prehadron cross section improves our previous computation [17]. The proton

spectra, however, cannot be described by the presented model adequately. We'll discuss this issue in Sec. 4.1.

### 3 Mass-number dependence

The dependence of hadron attenuation on the mass number  $A$  of the target nucleus is commonly believed to clearly distinguish the absorption and energy loss mechanisms for hadron attenuation. Indeed, the common expectation is that attenuation in absorption models is proportional to the hadron in-medium path length  $L$ , leading to  $1 - R_M \propto A^{1/3}$ . On the other hand, the average energy loss for a parton traversing a QCD medium is proportional to  $L^2$ , which leads to  $1 - R_M \propto A^{2/3}$ . In the following we will discuss in detail the  $A$ -dependence for the absorption model with the main goal to obtain insights via analytic formulae. A numerical analysis of the  $A$ -dependence is presented in Section 4.

For illustrative purposes and to obtain analytic formulae we take the model described Sec. 2 in the one step approximation where we neglect final hadron production in the calculation of the survival probability, since at  $z \geq 0.2$  the average hadron formation length is longer than 10 fm, as shown in Table 1. To further simplify, we consider the case of a hard-sphere nucleus of mass number  $A$  and radius  $R = r_0 A^{1/3}$ , with  $r_0 = 1.12$  fm [22]. We also consider only hadronization from rank 1 on, dominant in the HERMES kinematics except for  $K^-$  or  $\bar{p}$  production. Neglecting absorption in deuterium and the small rescaling correction we find that the hadron multiplicity ratio  $R_M$  equals the hadron survival probability  $S_A$ . Therefore, the hadron attenuation  $1 - R_M$  can be approximated as:

$$1 - R_M \approx 1 - S_A \\ = 1 - \frac{\pi \rho_0}{A} \int_0^{R^2} db^2 \int_{-R(b)}^{R(b)} dy \int_y^\infty dx \frac{e^{-\frac{x-y}{\langle l^* \rangle}}}{\langle l^* \rangle} e^{-\rho_0 \sigma_* \int_x^\infty ds \Theta(R(b) - |s|)}, \quad (20)$$

where we omitted all flavor and hadron species dependence for simplicity. In Eq. (20)  $\rho_0$  is the nuclear density,  $r_0 = \left(\frac{3}{4\pi\rho_0}\right)^{1/3}$  and  $R(b) = \sqrt{R^2 - b^2}$ . With the mean free path of the prehadron  $\lambda_* = 1/(\sigma_* \rho_0)$  the expression for the attenuation simplifies:

$$1 - R_M = \frac{\pi \rho_0}{2A} \langle l^* \rangle^3 \int_0^{2R/\langle l^* \rangle} dt t \int_0^t dr \int_0^r du e^{-u} \left[ 1 - e^{\frac{\langle l^* \rangle}{\lambda_*} (u-r)} \right] \quad (21)$$

The attenuation is controlled by two ratios; firstly,  $a = \langle l^* \rangle / \lambda_*$ , the ratio of formation length to mean free path and, secondly,  $b = 2R/\langle l^* \rangle$ , the size of

$z$	$\langle l^h(z) \rangle$ [fm]	$c_1$	$c_2$	$\bar{A}$
.25	10.15	0.0095	-0.000096	980
.45	11.72	0.0103	-0.000114	860
.65	12.34	0.0142	-0.000217	530
.85	11.98	0.0314	-0.001059	160

Table 1

Average hadron formation time and values of the  $c_1$  and  $c_2$  coefficients in Eq. (25) for  $\pi^+$  production at different  $z$  values. The mass number  $\bar{A}$  at which  $A^{4/3}$  terms in (25) become comparable with  $A^{2/3}$  terms are also given. For each value of  $z$ , we have taken the appropriate average value of  $\nu$  measured at [2]. The large value of  $\langle l^h \rangle > 10$  fm justifies neglecting hadron interactions with the nucleus.

the nucleus relative to the formation length. If both quantities are small one can expand the integrand in powers of  $u$ , obtaining after all the integrations a series which starts with  $b^2 \propto A^{2/3}$ , contrary to common expectations which dictate  $A^{1/3}$ :

$$1 - R_M = \frac{1}{10}ab^2 - \frac{1}{48}(1+a)ab^3 + \frac{1}{280}(1+a+a^2)ab^4 + \mathcal{O}[b^5]. \quad (22)$$

However, since  $a$  and  $b$  are of order unity for medium to heavy nuclei, the series converges very slowly, we cannot state whether or not it is possible to approximate the full expression by the leading term  $\propto A^{2/3}$ . To improve the convergence we fit the  $r$ -dependence of the integrand to a numerical function with a simpler form:

$$\int_0^r du e^{-u} \left[ 1 - e^{a(u-r)} \right] = \frac{1 - e^{-ar} - a(1 - e^{-r})}{1 - a} \approx 1 - e^{-war^2}. \quad (23)$$

A good fit can be achieved with a constant

$$w = 0.19 \quad (24)$$

independently of  $r$  and  $a = \frac{\langle l^* \rangle}{\lambda_*}$  in the range  $0 < r < 5$ ,  $0 < a < 3.5$  where the function differs substantially from zero. Using Eq. (23) in (21), one finds a rapidly converging expansion of the attenuation, since now the small  $w$ -parameter enhances the convergence:

$$\begin{aligned} 1 - R_M &= \frac{1}{5}wab^2 - \frac{3}{70}(wab^2)^2 + \mathcal{O}[(wab^2)^3] \\ &= c_1 A^{2/3} + c_2 A^{4/3} + \mathcal{O}[A^2]. \end{aligned} \quad (25)$$

We have computed the coefficients  $c_1$  and  $c_2$  in Eq. (25) for  $\pi^+$ -production and different values of  $z$ . The results are presented in Table 1. We observe that the

series converges quickly over the whole  $z$  range. Therefore, it makes sense to approximate the nuclear attenuation with a power law,

$$1 - R_M = cA^\alpha , \quad (26)$$

where

$$c \approx c_1(z) \quad (27)$$

$$\alpha \approx 2/3 \quad (28)$$

since higher-order terms will not give large corrections except at large  $z \gtrsim 0.8$ . Indeed from Eq.(25), we see that higher order terms are negligible if

$$A \ll \left| \frac{c_1}{c_2} \right|^{3/2} \equiv \bar{A} . \quad (29)$$

Values of  $\bar{A}$  are given in Table 1, and become comparable to mass numbers of medium-heavy nuclei around  $z = 0.8$ . We will further discuss the power-law fit (26) in Section 4.

We conclude with two remarks. First, a lot of information on absorption dynamics is contained in the proportionality coefficient  $c$  of Eq.(26), and its strong dependence on  $z$  needs to be taken into account when analyzing experimental data and theoretical models. Second, the approximate power law  $1 - R_M \propto A^{2/3}$  is not a peculiarity of the absorption model we developed, but has a more general validity. Indeed, it is possible to show that it appears whenever the probability distribution of the prehadron formation length  $\Delta y$  is analytic and has a finite limit as  $\Delta y \rightarrow 0$ . The origin of the  $A^{2/3}$  is geometric and related to the integration over the  $\gamma^*$ -quark interaction points. Non-analytic probability distributions may give leading powers different from 2/3.

## 4 Numerical results

### 4.1 Multiplicity ratio for $\pi$ , $K$ , $p$ and $\bar{p}$

The recent HERMES data have shown significant differences in the multiplicity ratios of various hadrons. As suggested in Refs. [13,14,16] the observed flavor-dependence of the multiplicity ratio may be useful to disentangle different theoretical frameworks describing the hadronization process. However, the aforementioned models provide computations for nuclear attenuation of charged hadrons [14], charged pions and kaons [13,16,8] only. Theoretical computations for protons and antiprotons, that are expected to be very sensitive to the formation length mechanism as shown in Fig. 3, are given in Ref. [10].

These predictions generally underestimate baryon multiplicity ratio, especially for the krypton nucleus and for  $z < 0.4$ .

In order to have charge-separated fragmentation functions, we use the leading order Kretzer parametrization [23] of the fragmentation functions for pions and kaons, while for protons and antiprotons we use the Kniehl-Kramer-Potter [24] parametrization. Predictions of our model for  $\pi^\pm$ ,  $K^\pm$ ,  $p$  and  $\bar{p}$  multiplicity ratios on He, Ne, Kr and Xe are shown for the  $z$  (Fig. 5) and  $\nu$  (Fig. 6) dependence, and compared to published HERMES data for identified hadrons on Kr [2] and to preliminary data on He [3] and Ne [3]. (We do not include computations and final data on N as they are very close to Ne.)

The  $z$  dependence reported in Fig. 5 shows nice agreement with the data for negative and positive pions for all the nuclei. The predictions for  $K^+$  and  $K^-$  are in qualitative agreement with the trend shown by the data, except for the low- $z$  region. This region contains contributions from both leading hadrons decelerated in nuclear rescattering and from secondary  $K^+$  and  $K^-$  produced from initial pions and  $\rho$ -mesons that are more abundant than strange particles. Both these contributions are not accounted in the purely absorption treatment of the final state interaction included in our model. The experimental  $z$  dependence of the antiprotons data is qualitatively reproduced within statistical uncertainties by the model, while the proton multiplicity ratio is underestimated especially in the low  $z$  region. The discrepancy at low- $z$  repeats itself in the  $\nu$ -dependence shown in Fig. 6, because an average  $z=0.3-0.4$  enters in the  $\nu$ -dependence. A simple explanation in terms of a smaller prebaryonic cross-section or a larger baryon formation is clearly insufficient to account for the large rise of the proton multiplicity ratio  $R_M^p$  above 1 at  $z \lesssim 0.4$ : indeed nuclear absorption can only reduce  $R_M$  below 1 and rescaling effects, which can increase  $R_M$  above 1 at low enough  $z$ , are too weak to describe the observed data. Another possible explanation for the difference in the proton sector is that theoretical computations do not account for the  $z$  degradation due to (pre)hadron rescattering nor final state interactions and decays. However, even a full transport model like Ref. [10,11] which takes these effects fully into account, fails to reproduce the rapid growth of the proton data at low  $z$ . In addition, the contribution of protons from target fragmentation is ruled out as an explanation of the effect, because the experimental momentum cut ( $|\vec{p}_N| > 4$  GeV) removes most of the protons knocked out of the nucleus. The discrepancy in the low- $z$  region may also point to a non negligible diquark contribution as suggested in Ref. [11].

## 4.2 Mass-number dependence: a new analysis

The simplest way of analyzing the  $A$ -dependence of hadron attenuation  $1 - R_M$  is in terms of a power law:

$$1 - R_M^h(z; A) = c^h(z; A) A^{\alpha^h(z; A)} . \quad (30)$$

For simplicity, we consider only hadron attenuation in fixed  $z$  bins, integrated over  $\nu$  and  $Q^2$ ; a similar discussion applies for arbitrary bins in  $z$ ,  $\nu$  and  $Q^2$ . The coefficients  $c$  and  $\alpha$  both depend in general on  $z$  and  $A$ . Indeed, as we have seen in section 3, the absorption model gives a power series: the lowest order term is  $A^{2/3}$ , but higher order terms become important for large  $A$  and  $z$ . Moreover, since we expect a strong dependence of the coefficient  $c$  on  $z$  a single constant  $c$  cannot fit all experimental bins. Therefore, we propose to analyze the  $A$ -dependence of our model and experimental data alike, by fitting the hadron attenuation to the power law (30) leaving both  $\alpha$  and  $c$  as free parameters. These parameters are strongly correlated: indeed a small increase of the exponent  $\alpha$  can be compensated by a small decrease of the coefficient  $c$ , and vice-versa. Therefore the fit results are best presented as  $\chi^2$  contour plots in the  $(c, \alpha)$ -plane, showing the aforementioned correlations.

The best-fit parameters  $c$  and  $\alpha$  are determined by chi-square minimization, i.e. the  $\chi^2$  merit function

$$\chi^2(c, \alpha) = \sum_i \frac{1}{\sigma_i^2} [(1 - R_M^h)(A_i) - c A_i^\alpha]^2 \quad (31)$$

is minimized with respect to  $c$  and  $\alpha$ . Here  $\sigma_i$  is the uncertainty of the theoretical or the experimental points respectively. For the experimental data we use the statistical uncertainty only, while in the case of the theoretical computations we use the quadratic sum of the uncertainties corresponding to the precision of the numerical computation ( $\approx 1\%$ ), and to the choice of model parameters. In our model we fit the value of the prehadron-nucleon cross section  $\sigma_*$  to experimental data for  $\pi^+$  production on Kr. Hence the theoretical relative uncertainty is determined by the experimental relative uncertainty of  $\pi^+$  attenuation on Kr, which approximately equals 6% independent of  $z$ . Then, we assume that the uncertainty of  $\sigma_*$  similarly yields a 6% relative uncertainty on hadron attenuation independently of  $z$  and  $A$ , as well. A change in the other parameters of the model would be reflected in a slightly different value of  $\sigma_*$ , but would not affect the estimate of the theoretical uncertainty of hadron attenuation.

The  $\chi^2$  contour plots in the  $(c, \alpha)$ -space are computed as constant  $\chi^2$  boundaries, enclosing a region such that

$$\chi_{min}^2 < \chi^2 < \chi_{min}^2 + \Delta\chi^2 \quad (32)$$

where  $\chi_{min}^2$  is the minimum of the  $\chi^2$  function, obtained at the best-fit parameters. We fix  $\Delta\chi^2 = 4.61$  which corresponds, in the case of normally distributed fit parameters, to the region which covers 90% of the total probability distribution.

The dotted  $\chi^2$  contours in Fig. 7 represent the fit to the numerical computation in various  $z$ -bins of the full theoretical model as it is described in section 2, including  $^4\text{He}$ ,  $(^{14}\text{N})$ ,  $^{20}\text{Ne}$  and  $^{84}\text{Kr}$  nuclei. In order to have a direct comparison with the theoretical mass number dependence analysis of the pure absorption model in section 3, the rescaling of parton distribution and fragmentation functions is not included in the numerical computation yielding the dashed contours. The solid  $\chi^2$  contours are obtained from the published HERMES data on  $(^{14}\text{N})$  [1] and  $^{84}\text{Kr}$  [2] and the preliminary data on  $^4\text{He}$  [3] and  $^{20}\text{Ne}$  [3]. The notation  $(^{14}\text{N})$  indicates that this nucleus is included in the fits of theory and experiment only for  $z \geq 0.55$ , because there are no experimental data in lower  $z$ -bins. The fits at  $z \leq 0.45$  contain only three data points, namely He, Ne and Kr, and 2 fit parameters. Therefore, the fit yields in these bins at best a rough estimate only. Hence, we consider the results in these  $z$  bins to be less reliable.

The presented results on He, (N), Ne and Kr at  $z \geq 0.55$  for the pure absorption model computation are qualitatively in agreement with the trend shown by the experimental data, except for the  $z = 0.85$  bin, where the experimental fit gives the largest  $\alpha$  due to  $1 - R_M < 0$  value for  $^4\text{He}$ . At small  $z$ , the full model contours behave similarly to the pure absorption contours, but the two become more and more separated as  $z$  is increased. Furthermore, the full model increasingly disagrees with experimental data when  $z \geq 0.75$ . This shows the power of the proposed kind of analysis, which is a possible tool to disentangle different theoretical models.

The slope of the  $\chi^2$  contour plots shows a trend to decrease by increasing  $z$ . In general, the slope of the contours in the  $(c, \alpha)$ -plane for the different  $z$ -bins is estimated by calculating the variation of  $1 - R_M^h = c\langle A \rangle^\alpha$  at an average mass number  $\langle A \rangle$ :

$$\Delta(1 - R_M^h) = \langle A \rangle^\alpha \Delta c + c \alpha \langle A \rangle^{\alpha-1} \Delta \alpha. \quad (33)$$

A change  $\Delta c$  of  $c$  is correlated with a corresponding change  $\Delta \alpha$  of  $\alpha$  given by

$$\Delta \alpha = -\frac{\langle A \rangle}{c \alpha} \Delta c. \quad (34)$$

z	Experiment		Theory		Theory	
	He (N) Ne Kr		He (N) Ne Kr		He (N) Ne Kr Xe	
	$c [10^{-2}]$	$\alpha$	$c [10^{-2}]$	$\alpha$	$c [10^{-2}]$	$\alpha$
.25	$2.1 \pm 0.7$ 0.4	$0.49 \pm 0.08$ 0.08	$0.8 \pm 0.8$ 0.5	$0.71 \pm 0.25$ 0.16	$1.5 \pm 0.7$ 0.9	$0.55 \pm 0.21$ 0.09
.35	$2.6 \pm 0.7$ 0.7	$0.47 \pm 0.08$ 0.07	$0.8 \pm 0.8$ 0.5	$0.74 \pm 0.26$ 0.17	$1.4 \pm 0.7$ 0.9	$0.56 \pm 0.22$ 0.09
.45	$1.7 \pm 0.9$ 0.4	$0.59 \pm 0.08$ 0.11	$0.8 \pm 0.8$ 0.5	$0.75 \pm 0.25$ 0.17	$1.4 \pm 0.7$ 0.9	$0.57 \pm 0.22$ 0.09
.55	$1.3 \pm 0.9$ 0.4	$0.65 \pm 0.10$ 0.14	$0.9 \pm 0.6$ 0.5	$0.73 \pm 0.14$ 0.12	$1.5 \pm 0.5$ 0.8	$0.58 \pm 0.16$ 0.08
.65	$1.7 \pm 1.2$ 0.6	$0.62 \pm 0.12$ 0.14	$1.1 \pm 0.7$ 0.5	$0.71 \pm 0.16$ 0.13	$1.7 \pm 0.5$ 0.9	$0.57 \pm 0.16$ 0.07
.75	$1.2 \pm 0.9$ 0.5	$0.74 \pm 0.14$ 0.14	$1.4 \pm 0.7$ 0.6	$0.69 \pm 0.15$ 0.11	$2.2 \pm 0.5$ 1.0	$0.55 \pm 0.15$ 0.06
.85	$0.6 \pm 1.3$ 1.3	$0.94 \pm 0.10$ 0.27	$2.0 \pm 0.8$ 0.8	$0.64 \pm 0.13$ 0.09	$3.0 \pm 0.6$ 1.4	$0.52 \pm 0.14$ 0.05
.95	$3.9 \pm 1.7$ 1.6	$0.55 \pm 0.14$ 0.11	$3.5 \pm 1.1$ 1.1	$0.56 \pm 0.11$ 0.08	$4.7 \pm 0.7$ 1.8	$0.46 \pm 0.12$ 0.04

Table 2

Centroids of the contour plots in Figs. 7 and 8 with their uncertainties for the fit  $1 - R_M = c(\nu, z, h)A^\alpha$  at fixed  $z$  bins, both for the experimental data and the pure absorption model calculation. The nuclei included in the fits are shown in the table, the parenthesis on (N) indicate that nitrogen is included in the fit only for  $z \geq 0.55$ . Note, that the theoretical results include different sets of nuclei.

This equation gives the negative slopes of the contours. As the product of  $c$  and  $\alpha$  generally increases with increasing  $z$ , this implies a decreasing slope.

The best-fit parameters, with their uncertainties are given in Table 2, both for the fits of the experimental data and the pure absorption model predictions. By showing the best-fit parameters of the pure absorption model computation we can quantitatively compare deviations from the leading order  $A^{2/3}$  dependence predicted in section 3. The uncertainties of the best-fit parameters are determined by projecting the contour plots on the  $c$ - and  $\alpha$ -axes respectively. Therefore, here as well, the parameter uncertainties correspond to a joined 90% confidence interval in the case of normally distributed parameters.

The values of  $\alpha$  derived from both the pure absorption model fits and the experimental fits on He,  $^{14}\text{N}$ , Ne, Kr at  $z \geq 0.55$  are compatible, within their uncertainties, with  $A^{2/3}$  behavior. Deviation from this behavior should be observed for heavier nuclei than krypton and at high  $z$  as shown in Table 1. In order to observe the breaking of the power law predicted by the model and to increase the statistical significance of the lowest  $z$ -bins, we perform the same computation by including xenon nucleus. Experimental data on Xe have been recently collected by the HERMES experiment, but the analysis is as yet in progress. The theoretical contour plots are shown in Fig. 8 and the best-fit parameters for the pure absorption model with their uncertainties

are summarized in Table 2. Since we include a nucleus with a mass number comparable to  $\bar{A}$  for large  $z$  bins, as shown in Table 1, the power law  $A^{2/3}$  is broken significantly producing a reduction of the  $\alpha$  values. This is clearly seen in Fig. 9, where the theoretical  $\alpha$  values in our pure absorption model are compared with the values derived from experimental data. The xenon nucleus significantly shifts the band of the theoretical predictions to lower  $\alpha$  values compared to the leading order  $\alpha = \frac{2}{3}$ . As different theoretical models may predict different values of  $\bar{A}$ , the presented analysis of the  $A$ -dependence of the hadron attenuation in nuclei is a promising tool in order to distinguish different theoretical assumptions.

## 5 Summary and conclusions

Rescaling of the structure and fragmentation functions together with (pre) hadronic absorption describe both HERMES and EMC data on the nuclear modification of hadron production in DIS processes [17]. This paper improves the original model of Ref. [17], by correctly evolving quarks, prehadrons and hadrons without factorizing the absorption process and hadronization processes. The hadron formation length is shown to be flavor dependent. Especially, negative kaons ( $K^- = s\bar{u}$ ) as well as antiprotons ( $\bar{p} = \bar{u}\bar{u}\bar{d}$ ) cannot be formed by a struck valence quark which is the dominant contribution at HERMES energy. This yields a smaller formation length for negative kaons and antiprotons implying more hadron suppression compared to positive kaons or protons respectively. Furthermore the so far neglected transverse extension of the produced hadrons leads to slightly different formation lengths for different hadron species. We now use a reasonable value for the string tension  $\kappa = 1$  GeV/fm, and extract the prehadronic cross-section  $\sigma_* = 2/3\sigma_h$  from data on pion production on krypton. This shows that the prehadron does not have the full hadronic size yet.

The presented model correctly describes pion and kaon multiplicity ratios. A different magnitude of the multiplicity ratios for positive and negative kaons originating from a flavor dependent formation length is reflected in the experimental data. In the baryon sector, although computed antiproton mutliplicities agree with experimental data inside their uncertainties, model computations disagree with proton data especially at small  $z$ . This discrepancy may be ascribed to a non negligible diquark fragmentation contribution in that region. Prehadron rescatterings and final state interactions are insufficient to fully account for the effect.

We have applied our model to the analysis of the mass number dependence of the hadron attenuation  $1 - R_M$ . Contrary to the common expectation we found a  $cA^{2/3}$  behavior in leading order, with higher order corrections increas-

ing in magnitude with increasing  $z$  and  $A$ . Hence, one must not expect a strict  $cA^{2/3}$  power law, but rather an effective behavior  $cA^\alpha$ . Furthermore, the proportionality coefficient  $c$  depends strongly on the kinematic variables, which rules out a simple analysis with a globally fixed  $c$ . Therefore we have proposed to analyze the  $A$ -dependence of hadron attenuation in terms of a power-law fit

$$1 - R_M = c A^\alpha \quad (35)$$

with both  $c$  and  $\alpha$  as fit parameters. Their correlations, displayed as  $\chi^2$  contours in the  $(c, \alpha)$ -plane, are quite sensitive to the underlying model assumptions and may disentangle different theoretical models.

Qualitative agreement is found between the theoretically and experimentally determined  $\chi^2$  contours, with  $\alpha \approx 2/3$ . Contrary to common expectations,  $\alpha \approx 2/3$  also in the presented absorption model. This value is not a peculiarity of our model, but a common feature of a quite large class of absorption models (a sufficient requirement being an analytic probability distribution in the formation length  $\Delta y$ , with a finite limit as  $\Delta y \rightarrow 0$ ). This fact bars the much advertised use of the exponent  $\alpha = 2/3$  as a direct experimental evidence of parton energy loss following the QCD "L<sup>2</sup>" law.

On the other hand, inclusion of a medium-heavy nucleus, like xenon, in our model introduces a sizable negative correction term which breaks the  $\alpha = 2/3$  power law, and shifts the value of the exponent to smaller values. This breaking is enhanced at large  $z$ . Recently collected data on xenon at HERMES will test this theoretical prediction.

In different models the breaking of the  $\alpha = 2/3$  power law happens at different values of  $A$  and  $z$ . Therefore collecting data up to heavy nuclei like Sn and Pb, which is in progress at Jefferson Laboratory with the CLAS experiment [25], will help unraveling the space-time dynamics of the hadronization process. The proposed analysis of the  $A$ -dependence of the hadron attenuation may thus provide a new method to differentiate between absorption and energy loss effects. In this respect we encourage the authors of competing models to perform a similar  $(c, \alpha)$  analysis to have a full set of predictions when the new data from HERMES and CLAS measurements will be available.

## Acknowledgments

We are grateful to P. Di Nezza, C. Ogilvie, J. Raufeisen and M. Rosati for fruitful discussions and many useful comments. This work is partially funded by the US Department of Energy grant DE-FG02-87ER40371 and by the European union project EU RII3-CT-2004-506078.

## References

- [1] A. Airapetian *et al.* [HERMES], Eur. Phys. J. C **20** (2001) 479.
- [2] A. Airapetian *et al.* [HERMES], Phys. Lett. B **577** (2003) 37.
- [3] G. Elbakian *et al.* [HERMES], Proceedings of the 11th International Workshop on Deep Inelastic Scattering (DIS 2003), St.Petersburg, April 23-27, 2003; V.T. Kim and L.N. Lipatov eds., page 597.
- [4] A. Bialas, Acta Phys. Polon. B **11** (1980) 475.
- [5] A. Bialas and M. Gyulassy, Nucl. Phys. B **291** (1987) 793.
- [6] A. Bialas and T. Chmaj, Phys. Lett. B **133** (1983) 241.
- [7] J. Czyzewski and P. Sawicki, Z. Phys. C **56**, (1992) 493.
- [8] N. Z. Akopov, G. M. Elbakian and L. A. Grigoryan, arXiv:hep-ph/0205123.
- [9] M. Gyulassy and M. Plumer, Nucl. Phys. B **346** (1990) 1.
- [10] T. Falter, W. Cassing, K. Gallmeister and U. Mosel, Phys. Lett. B **594** (2004) 61.
- [11] T. Falter, W. Cassing, K. Gallmeister and U. Mosel, Phys. Rev. C **70** (2004) 054609 and T. Falter, PhD thesis, Giessen University, 2004.
- [12] B. Kopeliovich, J. Nemchik and E. Predazzi, Proceedings of the workshop on Future Physics at HERA, Edited by G. Ingelman, A. De Roeck and R. Klanner, DESY, 1995/1996, vol 2, 1038 [nucl-th/9607036]. [arXiv:nucl-th/9607036].
- [13] B. Z. Kopeliovich, J. Nemchik, E. Predazzi and A. Hayashigaki, Nucl. Phys. A **740** (2004) 211
- [14] E. Wang and X. N. Wang, Phys. Rev. Lett. **89** (2002) 162301.
- [15] A. Majumder, E. Wang and X. N. Wang, arXiv:nucl-th/0412061.
- [16] F. Arleo, JHEP **0211** (2002) 044 and F. Arleo, Proceedings of 11th International Workshop on Deep Inelastic Scattering (DIS 2003), St. Petersburg, April 23-27, 2003, V.T. Kim and L.N. Lipatov eds. [arXiv:hep-ph/0309108]
- [17] A. Accardi, V. Muccifora and H. J. Pirner, Nucl. Phys. A **720** (2003) 131.
- [18] B. Andersson, G. Gustafson, G. Ingelman and T. Sjostrand, Phys. Rept. **97** (1983) 31.
- [19] G. Martens, C. Greiner, S. Leupold and U. Mosel, Phys. Rev. D **70** (2004) 116010 and Eur. Phys. J. A **18** (2003) 223.
- [20] O. Nachtmann and H. J. Pirner, Z. Phys. C **21** (1984) 277. R. L. Jaffe, F. E. Close, R. G. Roberts and G. G. Ross, Phys. Lett. B **134** (1984) 449; Phys. Rev. D **31** (1985) 1004. J. Dias de Deus, Phys. Lett. B **166** (1986) 98.

- [21] S. R. Amendolia *et al.*, Phys. Lett. B **146** (1984) 116. S. R. Amendolia *et al.*, Phys. Lett. B **178** (1986) 435. F. Borkowski, P. Peuser, G. G. Simon, V. H. Walther and R. D. Wendling, Nucl. Phys. B **93** (1975) 461.
- [22] B. Povh, K. Rith, C. Scholz, F. Zetsche: Particles and nuclei, 3. edition (Springer, Heidelberg 1995)
- [23] S. Kretzer, Phys. Rev. D **62** (2000) 054001.
- [24] B. A. Kniehl, G. Kramer and B. Potter, Nucl. Phys. B **582** (2000) 514.
- [25] W. K. Brooks, FizikaB **13** (2004) 321; B. A. Mecking *et al.* [CLAS], Nucl. Instrum. Meth. A **503** (2003) 513.

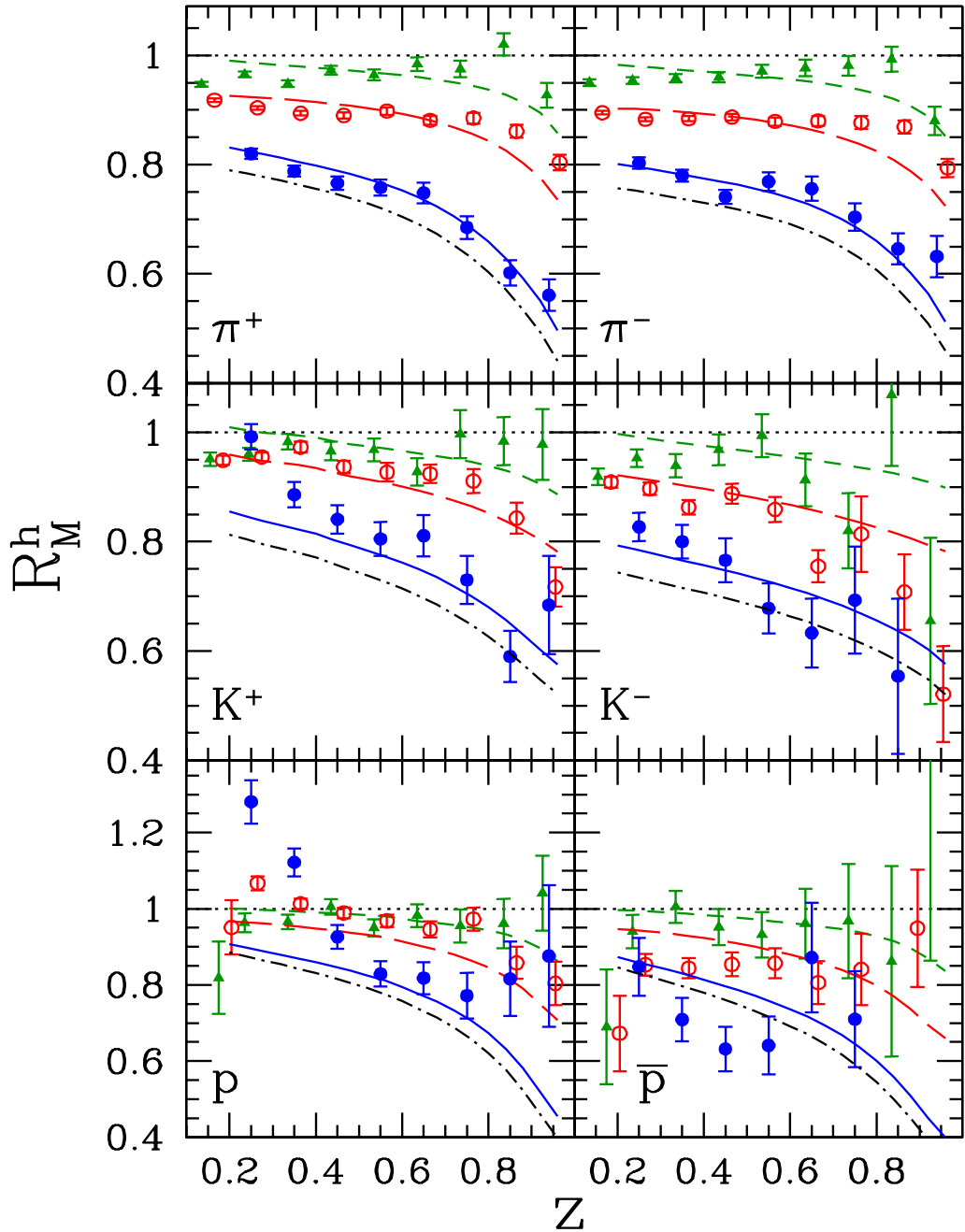


Fig. 5. Computed multiplicity ratios (cf. Eq. 1) for pions, kaons, protons and antiprotons as a function of  $z$  for He (dashed line), Ne (long-dashed line), Kr (solid line) and Xe (dot-dashed line). The HERMES data on Kr (solid circles) [2] and the preliminary data on He (closed triangles) and on Ne (open circles) [3] are shown with their statistical uncertainties. To improve the readability of the figure, He and Ne experimental points have been shifted by 0.015 to the left and to the right, respectively.

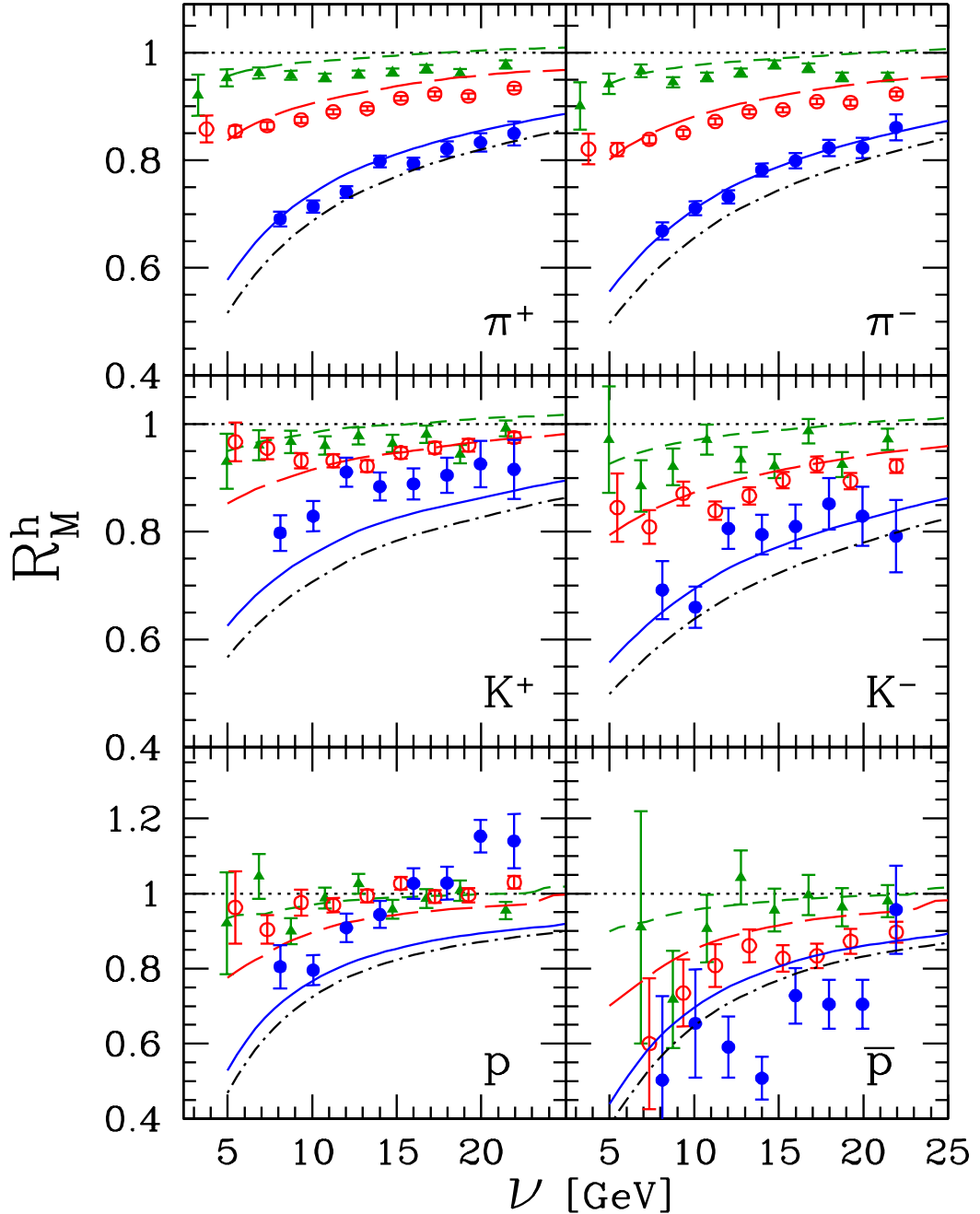


Fig. 6. Computed multiplicity ratios (cf. Eq. 1) for pions, kaons, protons and antiprotons as a function of  $\nu$  for He (dashed line), Ne (long-dashed line), Kr (solid line) and Xe (dot-dashed line). The HERMES data on Kr (solid circles) [2] and the preliminary data on He (closed triangles) and on Ne (open circles) [3] are shown with their statistical uncertainties. To improve the readability of the figure, He and Ne experimental points have been shifted by 0.25 GeV to the left and to the right, respectively.

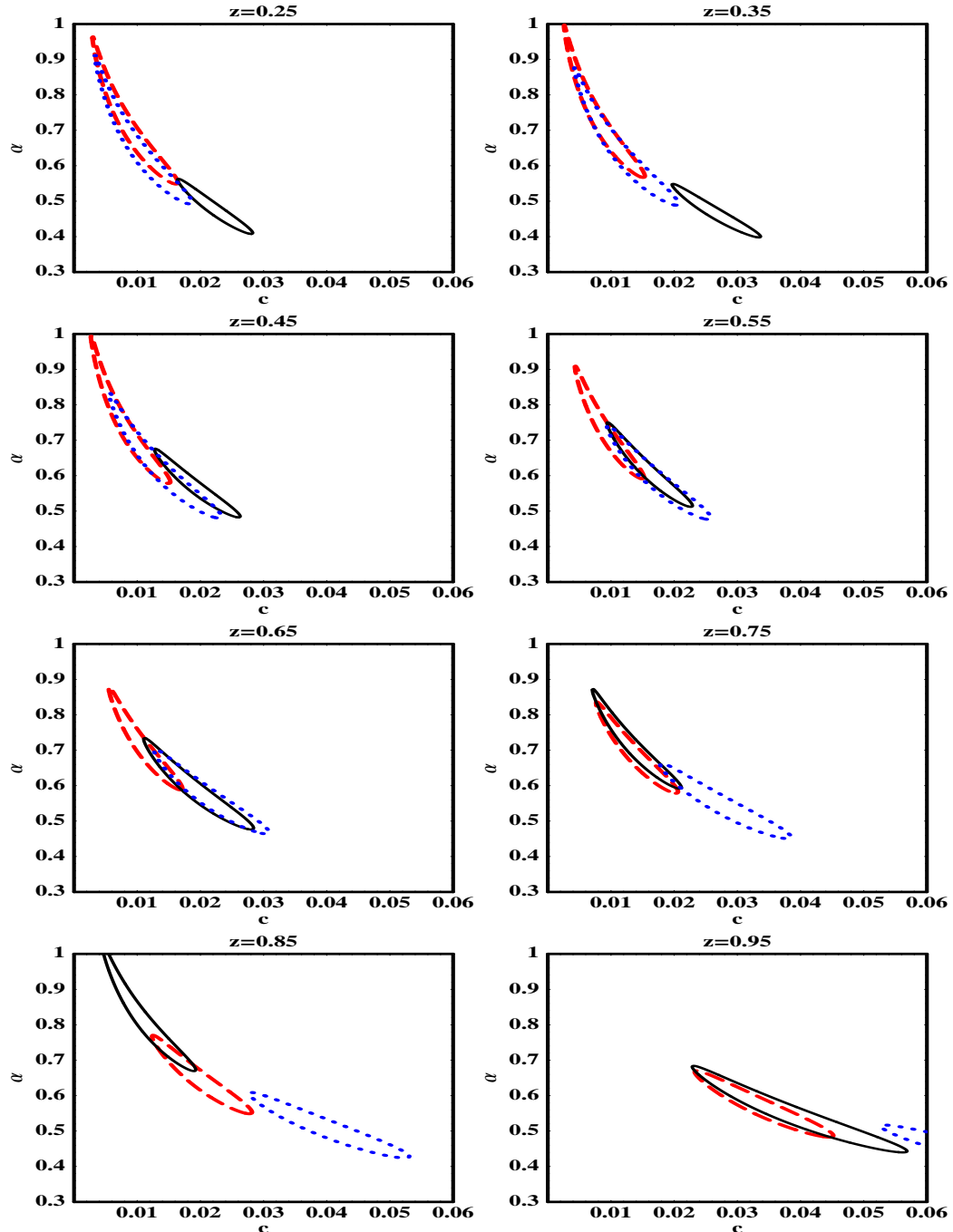


Fig. 7.  $\chi^2$  contours for the fit  $1 - R_M = c(\nu, z, h) A^\alpha$  on  ${}^4\text{He}$ ,  ${}^{14}\text{N}$ ,  ${}^{20}\text{Ne}$  and  ${}^{84}\text{Kr}$  nuclei, in fixed  $z$ -bins. The fits to our model computation are shown by the dashed  $\chi^2$  contours in the case of the pure absorption model and by dotted  $\chi^2$  contours in the case of the full model (absorption + rescaling). The solid contours show the fits to the HERMES pion multiplicity ratios on (N [1]), Kr [2] and to the preliminary data on He and Ne [3], accounting for statistical uncertainties only. The parenthesis on (N) indicate that nitrogen is included in the fit only for  $z \geq 0.55$ . Note that in the last  $z$  bin the contour for the full theory computation is partially out of the plot range.

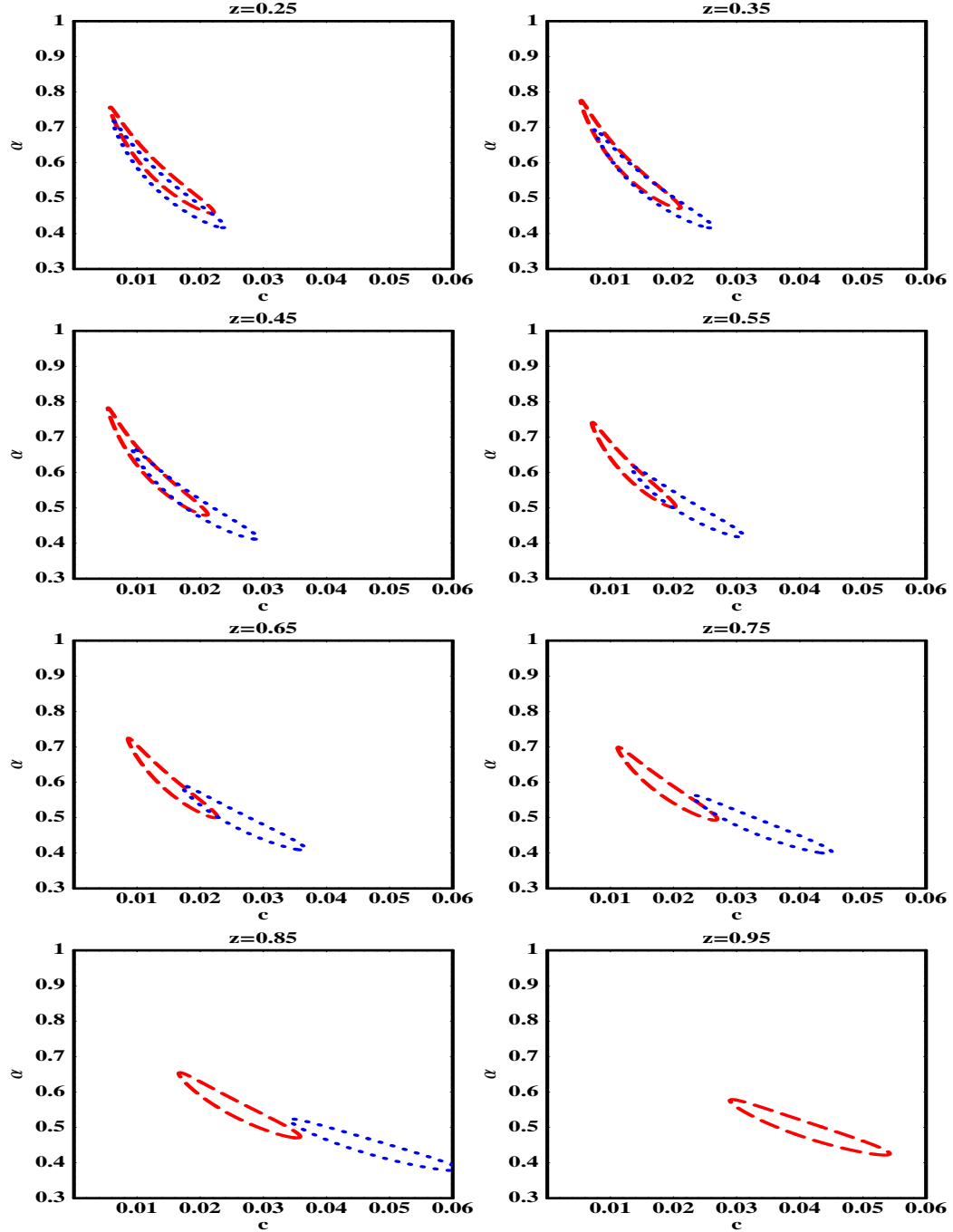


Fig. 8.  $\chi^2$  contour plots for the fit  $1 - R_M = c(\nu, z, h)A^\alpha$  on the pure absorption model (dashed) and the full model (dotted) computation for  $^4\text{He}$ ,  $(^{14}\text{N})$ ,  $^{20}\text{Ne}$ ,  $^{84}\text{Kr}$  and  $^{131}\text{Xe}$  nuclei, in fixed  $z$ -bins. Note that the contour for the full theory computation in the last  $z$  bin is outside of the plot range, to the right.

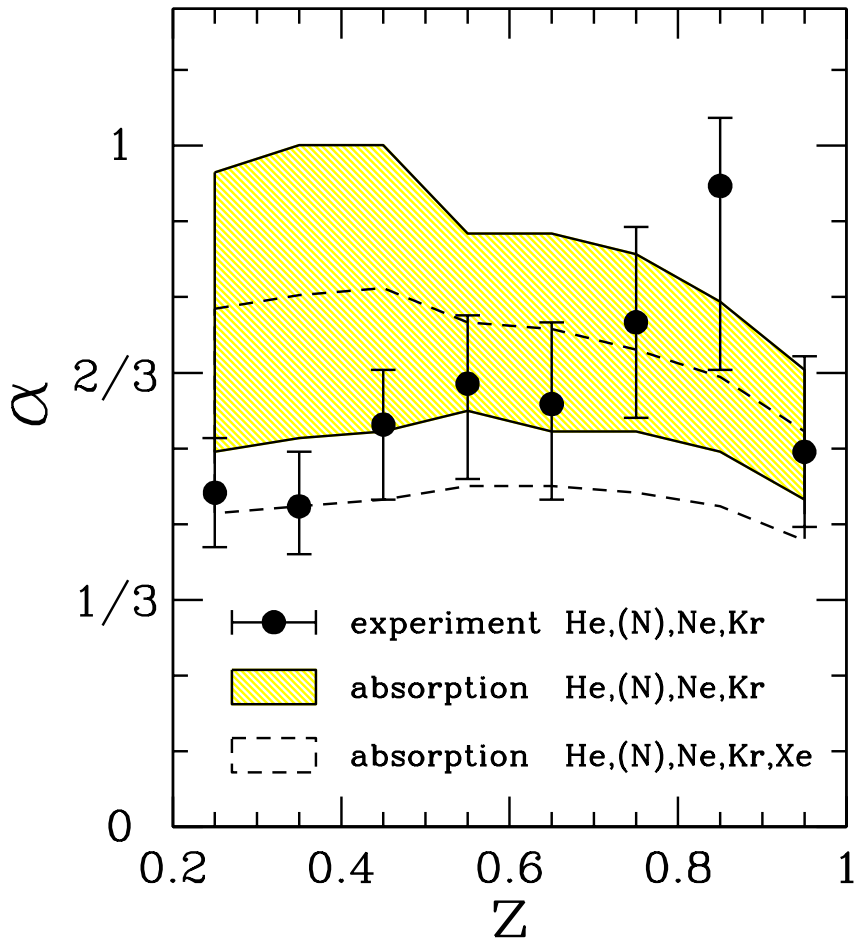


Fig. 9. Values of  $\alpha$  as a function of  $z$  derived from experimental data (dots) and our pure absorption model computation (bands). The nuclei included in the fit are shown in the legend (the HERMES data on He and Ne are preliminary). The notation (N) indicates that this nucleus is included in the fit only at  $z \geq 0.55$ . Note that experimental errors are uncorrelated, but theory errors are point-to-point correlated.